JOURNAL OF AIRCRAFT
Vol. 48, No. 1, January–February 2011

Optimization via FENSAP-ICE of Aircraft Hot-Air Anti-Icing Systems

M. P. C. Pellissier* and W. G. Habashi†
McGill University, Montreal, Quebec H3A 2S6, Canada
and
A. Pueyo‡
Bombardier Aerospace, Montreal, Quebec H4S 2A9, Canada

DOI: 10.2514/1.C031095

This paper presents a methodology for the optimization of hot-bleed-air anti-icing systems, known as Piccolo tubes. Such systems are widely used to anti-ice the wings of many commercial aircrafts, ranging from regional to wide-body jet aircrafts. Having identified the most critical in-flight icing conditions, as well as any anti-icing system constraints as inputs, the ideal aim is to achieve fully-evaporative conditions over the heated surfaces. To do so, an optimization method based on three-dimensional computational fluid dynamics, reduced-order models, and genetic algorithms was constructed to determine the optimal geometric configuration of the Piccolo tube (jet angles, spacing of jets, and distance from leading edge). The external and internal airflows are computed using the finite element Navier–Stokes applications package (FENSAP-ICE). The methodology leads to significantly-improved configurations for three- to five-dimensional design spaces.

Nomenclature

c	=	interjets spacing, m
c_p	=	specific heat, J/kg/K
d	=	Piccolo tube holes diameter, m
h_c	=	local heat transfer coefficient, W/m^2/K
k	=	thermal conductivity of the fluid, W/m/K
$\dot{m}$	=	local mass flow rate, kg/s
Nu	=	local Nusselt number based on Piccolo hole diameter, $Nu = h_c \cdot d/k$
nm	=	number of modes
ns	=	number of snapshots
p	=	penalty factor
$\dot{q}$	=	local heat flux, W/m^2
Re	=	jet Reynolds number , $Re = 4 \cdot \dot{m}_{\text{Jet}}/(\pi \cdot d \cdot \mu)$
r, R	=	radial distance from Piccolo jet axis, m
T	=	temperature, K
U_j	=	pod snapshot solution vector
$\hat{U}$	=	pod target solution vector
X_{Pic}, Y_{Pic}	=	position of the Piccolo tube axis inside the slat, m
z_n	=	normal distance from Piccolo hole to internal surface skin, m

Greeks

α_{ij}	=	pod snapshot coefficient
$\hat{\alpha}_{ij}$	=	pod target coefficient
θ_1, θ_2	=	jet orientation angles for the first and second row of Piccolo holes, deg
μ	=	dynamic viscosity, Pa.s
Φ_i	=	pod eigenfunction

Subscripts

anti-ice	=	anti-icing
cond	=	conduction
conv	=	convection
imp	=	impingement
in	=	coming in the control volume
jet	=	Piccolo Jets
kin	=	kinetic
out	=	coming out of the control volume
Pic	=	Piccolo tube
rb, R	=	runback

Presented as Paper 2010-1238 at the 40th AIAA Fluid Dynamics Conference, Orlando, FL, 4–7 January 2010; received 4 May 2010; revision received 1 September 2010; accepted for publication 1 September 2010.

*M.Eng., Department of Mechanical Engineering, Computational Fluid Dynamics Laboratory, 688 Sherbrooke Street West. Student Member AIAA.

†Ph.D., Chairholder and Director, Computational Fluid Dynamics Laboratory, Department of Mechanical Engineering, Natural Sciences and Engineering Research Council of Canada–J. Armand Bombardier–Bell Helicopter–CAE Industrial Research Chair for Multidisciplinary Computational Fluid Dynamics. Fellow AIAA.

‡Ph.D., Aero-Icing Lead, Advanced Aerodynamics Department, 2351 Boulevard Alfred Nobel.

I. Introduction

IN-FLIGHT icing is a major concern in aircraft safety because it remains a nonnegligible source of accidents and is still a serious hazard today [1,2]. Indeed, the aerodynamic performance of an aircraft flying in icing conditions can degrade rapidly and if not treated appropriately lead to incidents and accidents. In-flight icing occurs when an aircraft passes through clouds containing supercooled droplets at or below the freezing point [3]. Droplets impinge on its exposed surfaces and freeze, increasing drag and decreasing lift, eventually inducing flow separation and stall even at low angles of attack [4].

To avoid such events, aircraft are equipped with systems to prevent or remove ice accretion on critical aerodynamic surfaces; these devices must comply with flight safety regulations outlined by national certification authorities such as the Federal Aviation Administration [5], the European Aviation Safety Agency [6] and Transport Canada [7], among others. The most widely used anti-icing devices for wings and engine nacelles of commercial and corporate turbofan engine aircrafts are high-temperature bleed-air anti-icing systems, commonly called *Piccolo tubes*.

It is important to realize that safety has a significant cost. The amount of air bled from the engine for ice protection, along with conditioning and cabin pressurization can indeed represent 5 to 10%

of the core engine mass flow [8], half of which is for anti-icing purpose alone [9]. Additionally, air bleed induces engine performance penalties such as increase of specific fuel consumption, power loss and increase in turbine gas temperature [8,9]. The high bypass ratios and the ever-smaller core engine sizes of the modern turbofan engines make it crucial to maximize anti-icing system efficiency in order to minimize bleed-air.

In-flight icing and hot-bleed-air anti-icing topics are widely addressed in the literature. In terms of numerical models, computational fluid dynamics (CFD) simulations are performed for two-dimensional and/or three-dimensional configurations and in "dry-air" and/or "wet-air" conditions, coupling the external flow and internal flow solutions via conduction through the wing skin and conjugate heat transfer (CHT) framework [10–14]. To provide a more practical approach, experimental [15,16] and numerical [17] investigations of impinging jet arrays on a flat plate are carried out in order to elaborate heat transfer correlations. Also, to be more consistent with the hot-air anti-icing system geometry, numerical studies of impinging jet arrays on concave surfaces are performed [18,19] as well as experimental and numerical studies on hot-air anti-icing systems [20–22] to elaborate heat transfer correlations for anti-icing system design application. These correlations are used to replace the costly internal flow CFD computations to provide the heat transfer coefficient distribution at the wall. Moreover, experimental and computational investigations and parametric studies of hot-air anti-icing systems are carried out to evaluate the efficiency and performance of such systems, investigate their sensitivity to in-flight icing conditions and Piccolo tube geometric and thermodynamic parameters, as well as examine their behavior under off-design conditions [8,23–26].

The literature, however, is quite sparse with respect to the optimization of hot-bleed-air anti-icing systems. Santos et al. [25] performed a sensitivity analysis on a six-parameter internal flow correlation which was coupled with external flow, droplet impingement and ice accretion two-dimensional solvers. The sensitivity analysis methodology was developed to reveal the most significant geometrical and operational parameters of the hot-bleed-air anti-icing system in order to provide guidelines for parametric optimization. This methodology, which does not strictly speaking constitute an optimization procedure, relies on a Sobol design-of-experiments procedure and a response-surface-based reduced-order model (ROM) method. It was able to handle four geometric parameters and two thermodynamic parameters as design variables. Lastly, Saeed and Paraschivoiu [27] used a microgenetic-algorithm optimization code to determine the optimum Piccolo tube configuration for a given range of flight and icing conditions. This methodology relied on an internal flow two-dimensional correlation coupled with the two-dimensional icing code CANICE and managed two geometrical independent parameters and one thermodynamic independent parameter as design variables. The preliminary results suggested that genetic-algorithm-based optimization has significant application potential for the design of hot-air anti-icing systems.

Flight and wind-tunnel tests are also performed to investigate the behavior of anti-icing systems. On the one hand, however, flight-testing in natural icing conditions is expensive, dangerous and not all conditions outlined in the FAR-25 and the CS-25 can be replicated. On the other hand, icing-wind-tunnel-testing is costly and somewhat limited in its capacity of optimization. Both approaches are suitable for the evaluation of a system but constitute a costly and limited design platform. Therefore, the logical choice is to use CFD to model and optimize anti-icing systems before testing. Nevertheless, three-dimensional fully-coupled simulations (three-dimensional external flow, droplets impingement and ice accretion; three-dimensional conduction through the skin; three-dimensional internal flow; CHT) are quite demanding in terms of computing resources. Under such conditions, exploring the design space to come up with an optimal design would require a large number of CFD simulations and would not be cost-effective.

This paper's motivation is to develop a Piccolo tube optimization methodology based on genetic algorithms (GAs) able to handle three to five design variables. The associated models are three-dimensional CFD-based and include solving for the water runback. A ROM, such as proper orthogonal decomposition (POD), is used to limit the number of necessary computations. This approach focuses, for the moment, on single-objective optimization based on geometric parameters. The paper will first present the optimization methodology, second describe the different modules, third provide results and finally outline some recommendations for future work.

II. Parameterization

A. Geometry of the System

The three-dimensional swept constant chord model and Piccolo tube anti-icing system initial design, shown in Figs. 1 and 2, is a generic model provided by Bombardier Aerospace and for which experimental data are available [28]. The Piccolo tube is an integrated system mainly composed of a perforated tube located at the leading edge of the wing, inside the slat, as shown in the close-up in Fig. 3. This tube is perforated by two or three rows of small holes, usually arranged in a staggered manner, oriented to blow hot air onto the slat's inner surface.

The system is fed by hot air collected from the engine's first compressor, which is distributed along the wing slat by the Piccolo tube. The air is projected through the Piccolo holes toward the slat's inner surface of the front bay before flowing through the slot toward the rear bay and then out through the exhaust, as illustrated in Fig. 4 (adapted from Planquart et al. [20]).

B. Parameterization of the Problem

In the perspective of single-objective optimization, the proposed approach considers a single combination of flight configuration (ambient pressure, air speed, angle of attack) and in-flight icing condition [ambient temperature, liquid water content (LWC), droplets size], based on maximum total catch rate for holding

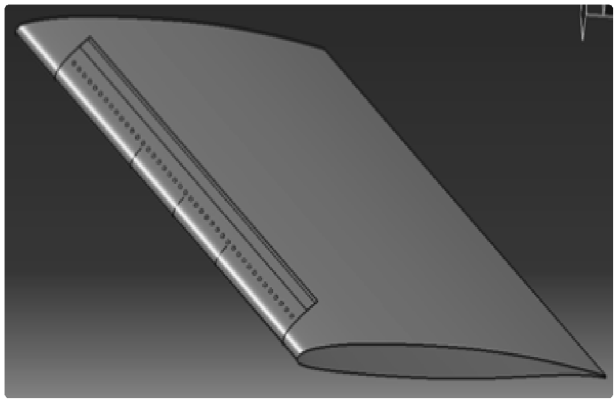

Fig. 1 Three-dimensional swept wing portion.

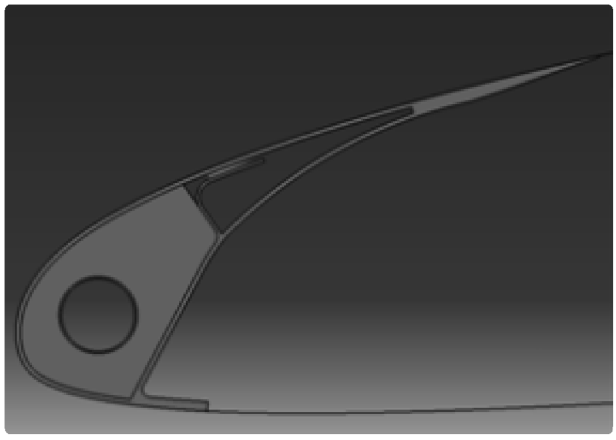

Fig. 2 Piccolo tube section on the wing slat.

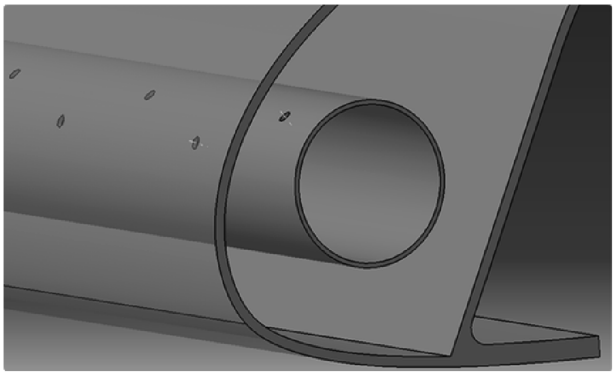

Fig. 3 Piccolo tube geometric configuration.

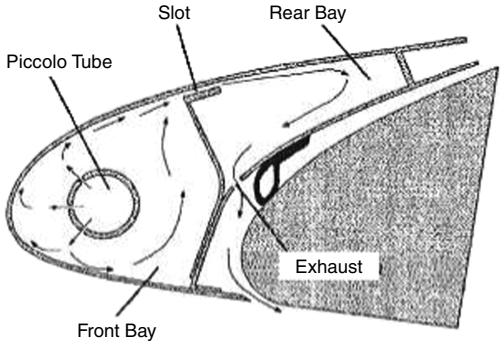

Fig. 4 Sketch of a slat hot-air anti-icing system section.

condition. This particular flight condition is considered to be one of the most adverse design points. The preceding parameters, along with the corresponding available anti-icing power (bleed-air mass flow, total pressure and temperature) were chosen as a generic yet realistic design point.

As a proof of concept, five geometric parameters were considered as design variables, as shown in Fig. 5: 1) the Piccolo tube horizontal and vertical positions: 20 mm $\leq X_{\text{Pic}} \leq$ 30 mm and -1.5 mm $\leq Y_{\text{Pic}} \leq 8$ mm; 2) the jet angle for each of the two rows: $-60^\circ \leq \theta_1 \leq 0^\circ$ and $0^\circ \leq \theta_2 - \theta_1 \leq 45^\circ$; and 3) the spacing between adjacent holes: 25 mm $\leq c \leq$ 75 mm.

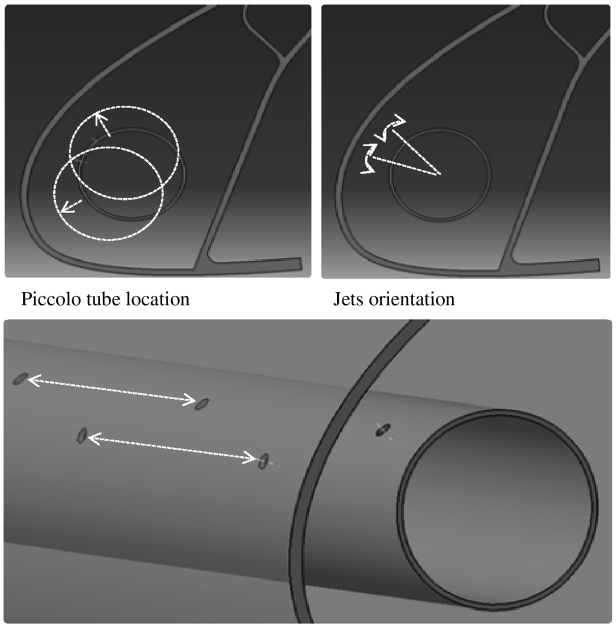

Fig. 5 Geometric parameters.

The Piccolo tube diameter, the number of rows, and the Piccolo jets hole diameter were fixed. The Piccolo thermodynamic parameters (i.e., air temperature and available mass flow) were also given.

III. Optimization Methodology

A. Overview

The optimization methodology is illustrated in the diagram of Fig. 6. It is designed in a modular fashion to allow for easy upgrading of any module independently. Each module is represented with a plain line. The inputs are represented in doted lines, while the final output is represented in semidotted line. The arrows represent the flow of data and the links between the different modules. The left module refers to the external flow simulation. Using the identified most critical case for the in-flight icing conditions, the three-dimensional external flow and associated droplet impingement solutions are computed. The middle module refers to the internal flow simulation. Given the Piccolo system inputs, the three-dimensional internal flow is computed and provides the corresponding anti-icing heat transfer coefficient distribution. Combining these entries into the water film model module, a water runback solution is computed. A set of water runback solutions, obtained for different sets of design variables, is previously computed to constitute the snapshots database of the POD module. The optimization core of the methodology, on the right side of the diagram, is composed of a GA module coupled with POD-based ROM module.

A description of these modules as well as the different models used in the methodology is presented in the following sections.

B. Genetic Algorithm

GAs, used as optimization tools, were inspired by evolution and natural selection theories which advocate the survival of the fittest individual. The term individual refers here to a particular set of design variables, encoded as a chromosome. From an initial group of individuals, referred as the population, some of the best individuals are selected to perform reproduction which lead to a new generation [29,30]. This recursive procedure is repeated until convergence, leading to the fittest individual, i.e., the global optimum, as illustrated in Fig. 7. The idea is to keep diversity to avoid local extrema, while limiting the population size or number of generation to get reasonably fast convergence [31].

GA are widely used as a single- or multiobjective global optimization strategy involving CFD [32,33]. It is frequently coupled with interpolation techniques, such as Kriging [34–36], specially in the case of large multidimensional design space, where they perform better than other optimization methods [37]. In this project, the GA module of the MATLAB optimization toolbox was used.

Generally, a GA population of 30 individuals for 50 generations leads to 1500 evaluations and thus 1500 associated computations. To run the optimization loop in reasonable time, the optimization procedure relies on POD-computed solutions to explore the wide

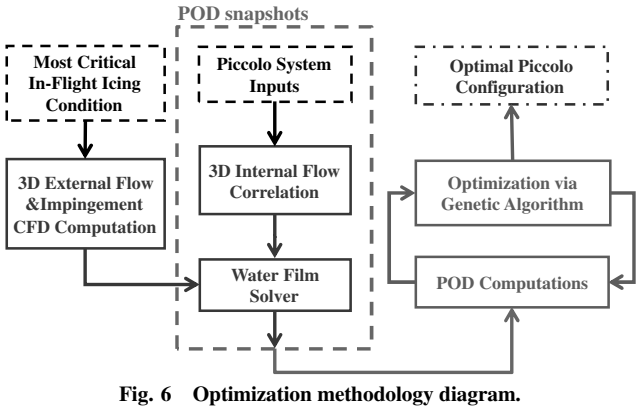

Fig. 6 Optimization methodology diagram.

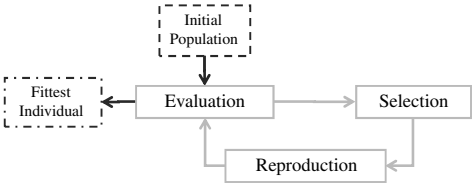

Fig. 7 GA procedure.

multidimensional design space. Using fully three-dimensional CFD computation for the internal flow and water film model requires 30 h per run and using correlation and water film model requires 5 min per run, whereas using POD computation brings the computational time down to 15 s per run.

C. Objective Function

To compare individuals, the GAs procedure involves evaluating each of them by means of an objective function (or "cost" function) closely related to the intrinsic specifications of the system. In the case of a thermal anti-icing system, the ideal aim is clearly to achieve the evaporation of all the impinging water, on both upper and lower surfaces, within the heated area. This means that there should be no water running back past the limits of the heated zone. It is possible that more than one configuration lead to fully-evaporative conditions on both upper and lower surfaces. In such case, the most energy efficient configuration would be chosen, i.e., maximizing the actual transferred anti-icing power to the potential total anti-icing power ratio:

$$\begin{aligned}\text{ObjFct} &= (\dot{q}_{\text{Anti-ice}} - \dot{q}_{\text{Vap}})/\dot{q}_{\text{Ref}} \\ &= (\dot{q}_{\text{Anti-ice}} - \dot{q}_{\text{Vap}})/[\dot{m}_{\text{Pic}} \cdot c_p \cdot (T_{\text{Pic}} - T_\infty)] \end{aligned} \quad (1)$$

In a real-world situation, it may be technically difficult and costly to achieve fully-evaporative over the entire slat in all in-flight icing conditions; either the system is inadequate under exceptional conditions like supercooled large droplets, or more simply other constraints come into the picture such as the maximal temperature the slat material can bear on a hot day case if the anti-icing system is accidently activated, or even in the case of limited available bleed air. In such a case, anti-icing systems do not always guarantee fully-evaporative conditions on both upper and lower surfaces.

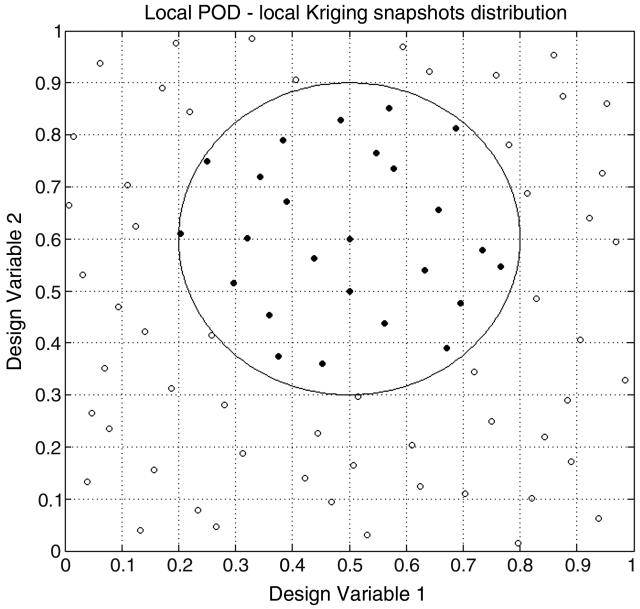

Fig. 8 Illustration in two-dimensional of the concepts of local POD and local Kriging.

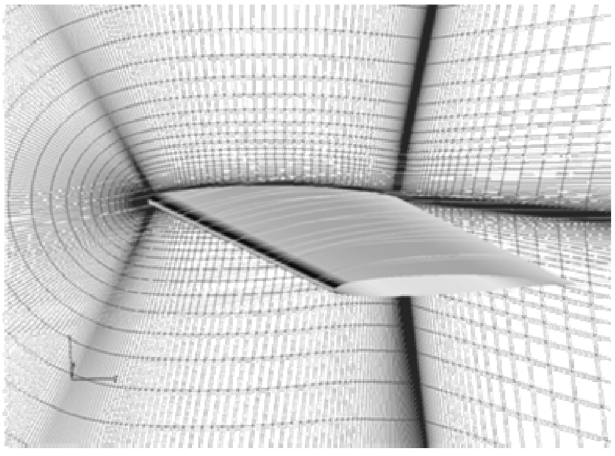

Fig. 9 Three-dimensional flow streamlines around swept wing.

Fig. 10 Corresponding droplet impingement.

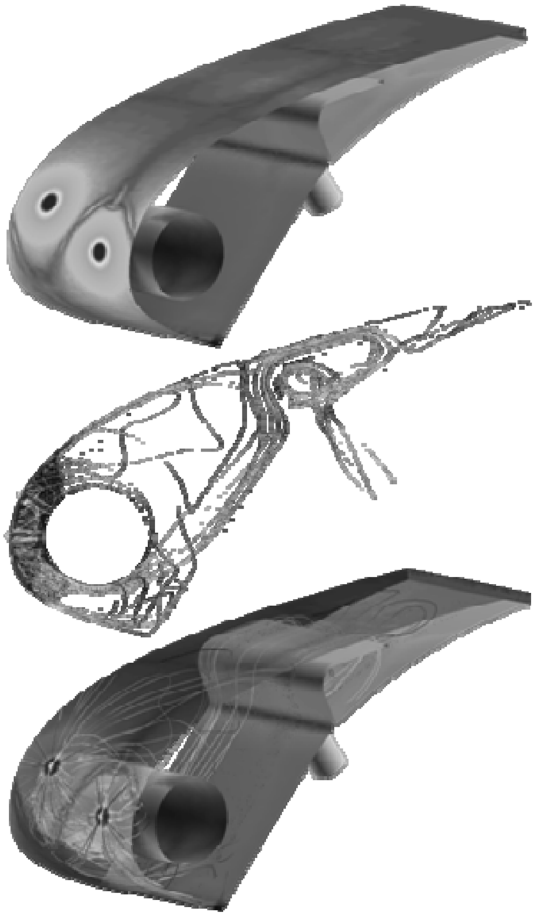

Fig. 11 Three-dimensional internal flow inside the slat.

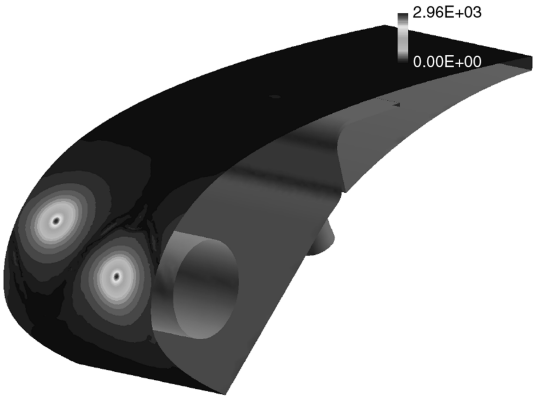

Fig. 12 Internal heat transfer coefficients surface distribution from CFD.

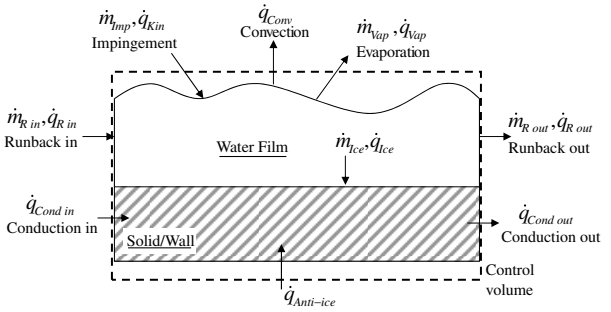

Fig. 13 Water film model mass and energy balance over a control volume.

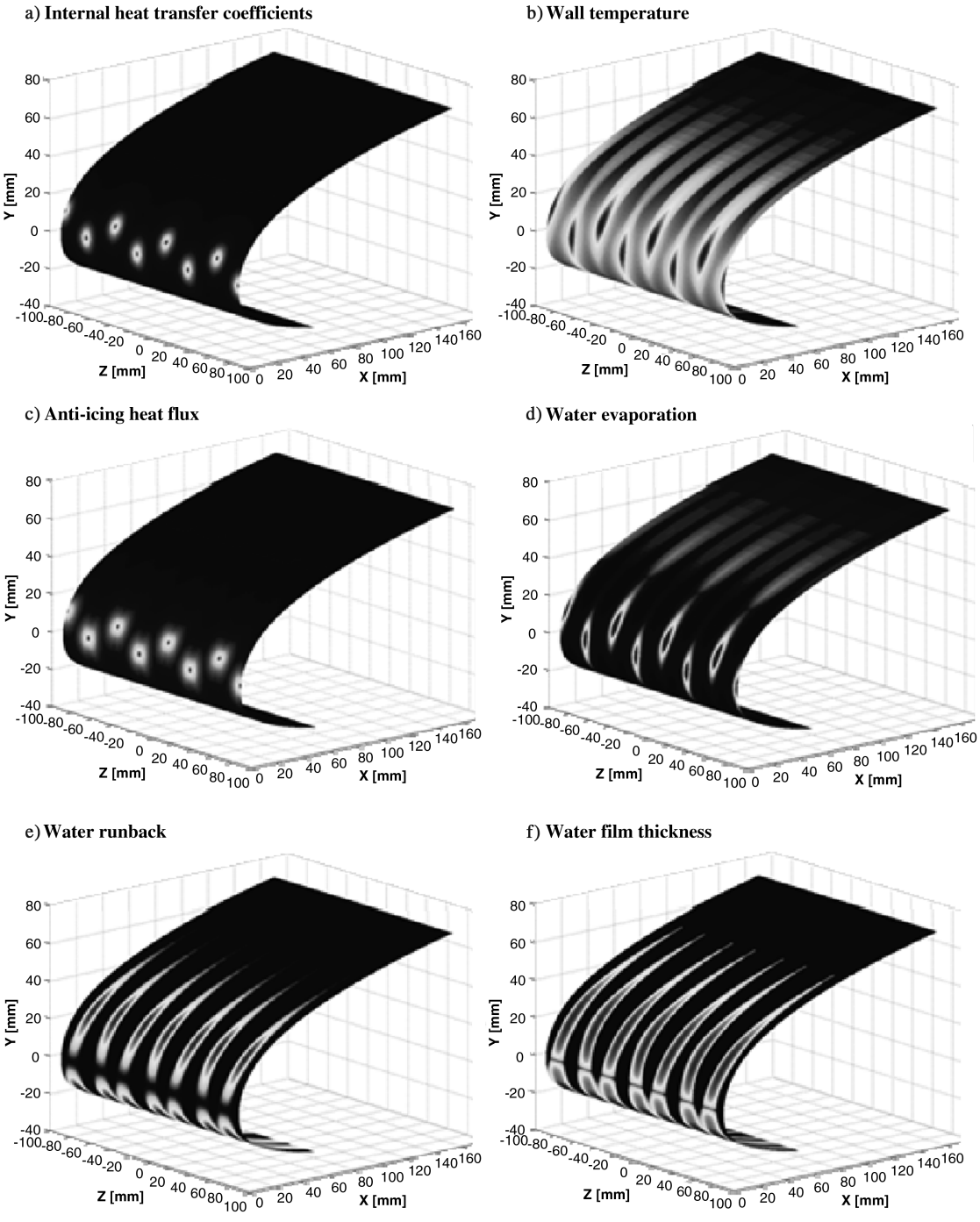

Fig. 14 Example of water film solution.

The anti-icing power is concentrated to ensure that the upper surface of the slat reaches fully-evaporative conditions (where the aerodynamics is more critical), while allowing a minimum amount of runback on the lower surface. Therefore, the optimization criterion is adapted consequently and can be reformulated as follows: from given available anti-icing power, minimize the water runback on the lower surface of the slat while enforcing fully-evaporative condition on the upper surface, within the range of the design parameters.

Therefore, the cost function is defined as the global wasted power to global available power ratio (where the wasted power is simply the power that was not used for evaporation purposes) including a penalty term penalizing the runback on the upper surface:

$$\text{ObjFct} = (\dot{q}_{\text{Ref}} - \dot{q}_{\text{Vap}} \cdot e^{-p})/\dot{q}_{\text{Ref}} = 1 - \dot{q}_{\text{Vap}} \cdot e^{-p}/\dot{q}_{\text{Ref}} \quad (2)$$

The penalty term p is expressed as a function of the runback mass flow rate from the upper surface.

D. POD Computations

Reduced-order modelling, such as POD, has already been applied in the field of CFD [38,39] and is increasing in popularity, especially in the context of CFD-based optimization [40,41]. POD seeks to reconstruct an intermediate solution from a set of previously computed solutions or snapshots [42–44]. Any snapshot can be decomposed as a linear combination of basis functions and associated coefficients:

$$U_j = \sum_{i=1}^{ns} \alpha_{ij} \cdot \Phi_i \quad (3)$$

The basis functions, or eigenfunctions, are extracted from the eigenvalue problem associated to the cross-correlation matrix related to the combined snapshots. As the vector space spanned by the basis functions is orthonormal by definition, each coefficient is simply the dot-product of the corresponding eigenfunction with the snapshot itself. The target solution is also expressed as a linear combination of the basis functions:

$$\hat{U} = \sum_{i=1}^{nm \le ns} \hat{\alpha}_i \cdot \Phi_i \quad (4)$$

In this paper, the current ROM module is based on the POD-Kriging code developed by Lappo and Habashi [45]. Additional features were implemented in order to improve the accuracy and, more important, the speed. These features can be defined as local POD—local Kriging and are illustrated in Fig. 8.

In this two-dimensional design space, the blue dots represent the snapshots, uniformly distributed over the design space using the Lp-τ space filling method [46–48]. The center of the circle represents the target solution to be computed with POD. The POD model is then built from a set of closest snapshots, represented as the dots within the circle. The target's linear combination coefficients are then interpolated using Kriging also from the set of snapshots.

IV. Numerical Models

A. External Flow Computation

The three-dimensional external flow and associated droplet solution were computed using state-of-the-art CFD simulation tools [49]. Figure 9 illustrates the three-dimensional external flow computed by the finite element Navier–Stokes applications package (FENSAP) around the swept wing. It shows three-dimensional periodic flow streamlines around the airfoil and the pressure distribution over the surface. At the wing root is shown a two-dimensional slice of the three-dimensional structured mesh. Figure 10 illustrates the droplet impingement computed by DROP3D. It shows the collection efficiency distribution on the wing surface and at the wing root a two-dimensional slice of the three-dimensional LWC distribution. The constant chord swept wing is limited at both ends by periodic boundary conditions. In the context of single-objective optimization, the external flow and water impingement solution are computed once for the conditions mentioned in Sec. II.B. Here, the Spalart–Allmaras one-equation turbulence model was chosen.

B. Internal Flow Computation

Figure 11 illustrates the three-dimensional internal flow solution, also computed using FENSAP. The top picture shows the anti-icing heat flux distribution on the slat's surface. The other two pictures show the internal flow streamlines, which reveal highly three-dimensional features. The internal fluid domain is constituted by the smallest periodic pattern, delimited on each side by periodic boundary conditions. An arbitrary temperature distribution is imposed on the exchange surface, and an adiabatic condition on the other surfaces.

A sensibility analysis was carried out, which revealed relatively weak dependence on wall temperature, as far as the heat transfer coefficient distribution at the wall is concerned, for both external and internal flow computations [50]. This is a good motivation to decouple external and internal flow computations, meaning that they are computed separately [51], and benefit from the reduction in computational cost. In fact, solving for the complete coupled

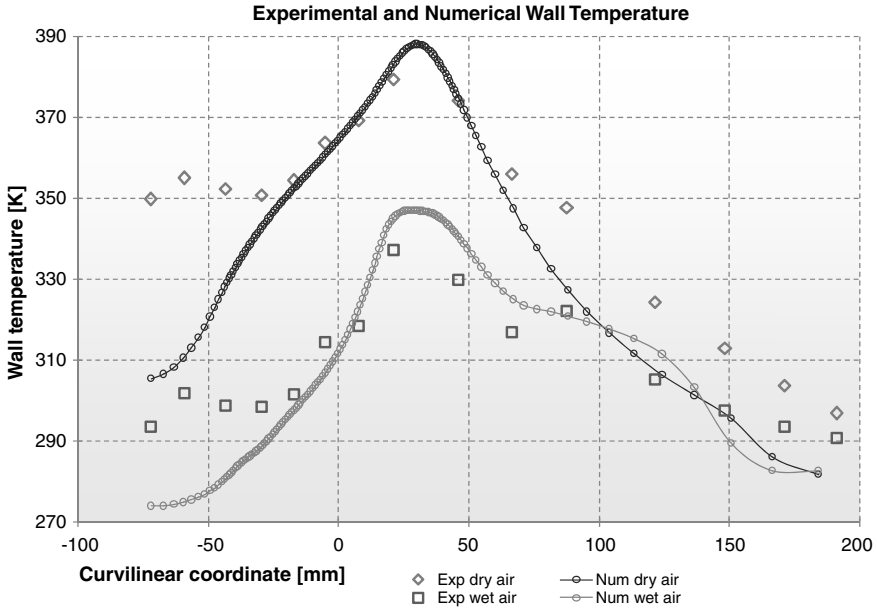

Fig. 15 Experimental and numerical icing test results.

problem within the optimization framework would not be affordable today.

C. From Three-Dimensional Simulation to Three-Dimensional Correlation

To reduce computational time and cost, and given that the heat transfer coefficient is the only field of interest extracted from internal flow computations, the internal flow three-dimensional CFD simulations were replaced by three-dimensional impinging jet correlations. The heat transfer coefficient distribution on the internal skin is obtained, based on an average Nusselt number correlation determined by Goldstein et al. [52]. This strategy was mentioned by Wright [21] and used by Lee et al. [12]. The correlation is presented in Eq. (5):

$$\overline{Nu}\Big|_{r=0}^{R} = Re^{0.76}(24 - |(z_n/d) - 7.75|)/(533 + 44 \cdot (R/d)^{1.285}) = 2/R^2 \cdot \int_0^R Nu(r) \cdot r \cdot \mathrm{d}r \tag{5}$$

where Re is the Reynolds number based on the hole diameter d, r is the radial distance from the impinging jet stagnation point on the wall and z_n is the normal distance from the hole to the wall. The correlation was developed for a Reynolds number up to 124,000, a normal distance from 6 to 12 hole diameters, and a radial distance up to 32 hole diameters. Importantly, this correlation was developed for a single jet impinging on a flat plate, however, it was one of the very few correlations that could provide the average Nusselt number as an explicit function of the radial distance [21]. The local Nusselt number is recovered from the expression of the average Nusselt number and the corresponding local heat transfer coefficient is obtained:

$$h_c(r) = Nu(r) \cdot k/d \tag{6}$$

The preceding correlation was actually adapted to the current problem and fitted to three-dimensional CFD simulations of the internal flow for different geometric configurations using FENSAP (see Fig. 12). Thus, the curvature of the impinged surface and, to some extent, the interaction between jets are better accounted for. The CFD-computed heat transfer coefficients are obtained from the convective heat flux at the wall and the temperature difference between the reference Piccolo temperature and the local wall temperature.

The gain in terms of computational time is considerable. Indeed, the correlation takes less than 1 s to compute, as opposed to the internal three-dimensional CFD computation on a 64-CPU cluster which requires 30 h to run.

D. Water Film Model

The water runback and surface temperature distributions were computed using a quasi-one-dimensional finite volume model solving for the mass and energy balances on the water film, along two-dimensional cuts. This model, illustrated in Fig. 13, is based on the water film thermodynamic analysis which was first introduced by Messinger [53], and further improved for aircraft icing [54,55].

The impinging water mass flux and the external heat transfer coefficient distribution are extracted from the three-dimensional external flow and droplet impingement solutions. The internal heat transfer coefficient distribution is computed using the correlation. The water film model consists in a local mass and energy balance, solving for local steady-state wall temperature and water runback mass flow rate along the skin in the streamwise direction over the airfoil surface.

The mass balance is expressed as follows:

$$\dot{m}_{\mathrm{IN}} = \dot{m}_{R\mathrm{in}} + \dot{m}_{\mathrm{Imp}} = \dot{m}_{R\mathrm{out}} + \dot{m}_{\mathrm{Vap}}(+\dot{m}_{\mathrm{Ice}}) = \dot{m}_{\mathrm{OUT}} \tag{7}$$

where $\dot{m}_{rb}$ is the water runback mass flow rate that passes through the control volume, $\dot{m}_{\beta}$ is the impinging mass flow rate and $\dot{m}_{\mathrm{evap}}$ is the evaporative mass flow rate.

The energy balance is expressed as follows:

$$[\dot{q}_R]_{\mathrm{in}}^{\mathrm{out}} + \dot{q}_{\mathrm{Kin}} + \dot{q}_{\text{Anti-ice}} + [\dot{q}_{\mathrm{Cond}}]_{\mathrm{in}}^{\mathrm{out}} - \dot{q}_{\mathrm{Vap}} - \dot{q}_{\mathrm{Conv}} - \dot{q}_{\mathrm{Rad}}(+\dot{q}_{\mathrm{Ice}}) = 0 \tag{8}$$

where $\dot{q}_R$ is the water runback enthalpy, $\dot{q}_{\mathrm{Imp}}$, $\dot{q}_{\text{Anti-ice}}$, $\dot{q}_{\mathrm{Cond}}$, $\dot{q}_{\mathrm{Vap}}$, $\dot{q}_{\mathrm{Conv}}$ and $\dot{q}_{\mathrm{Rad}}$ are, respectively, the heat fluxes due to kinetic energy

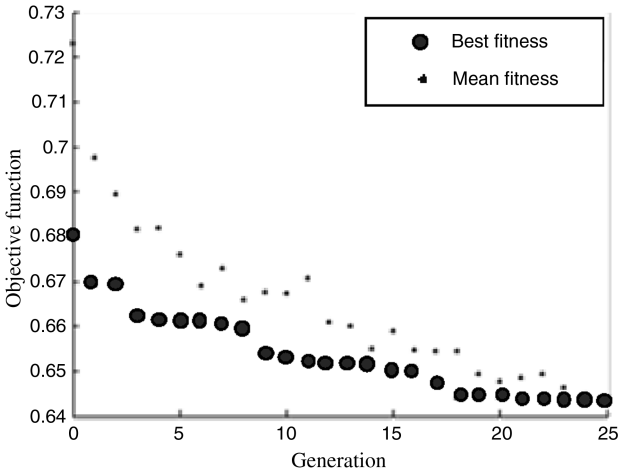

a) Mean and best fitness values

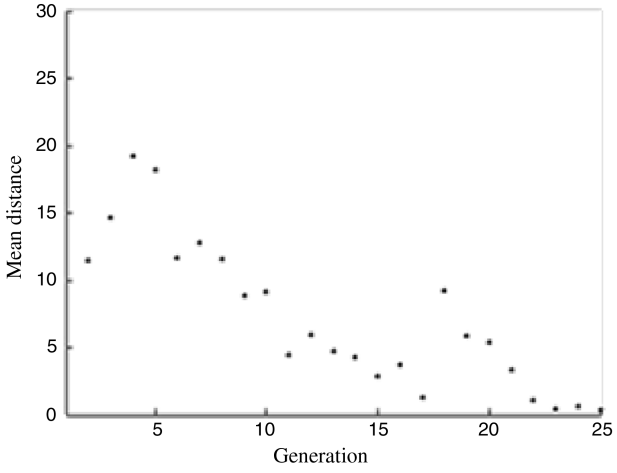

b) Mean distance b/w individuals

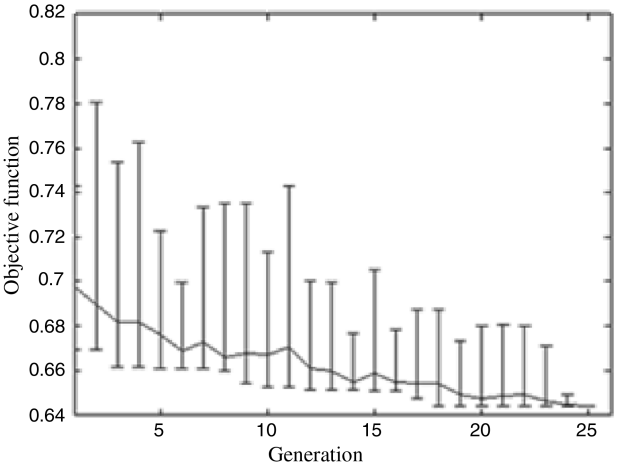

c) Mean and range of fitness values

Fig. 16 GA convergence.

of impinging droplets, internal convection, conduction, evaporation, external convection and radiation.

On the one hand, the water film thickness is very small (of the order of tens of microns). On the other hand, the skin thickness is relatively small and its thermal conductivity high (about 2 mm of aluminum). Therefore, the temperature difference across the water film and across the metal skin can be ignored. Thus the local temperature is considered uniform in each control volume. For simplicity, all physical and thermodynamic variables are considered constant within a given control volume.

E. Water Film Solution

Figure 14 illustrates an example of water film solution in the case of non-fully-evaporative conditions. In this case, evaporative state is reached on the upper surface. Figure 14a displays an example of correlated internal heat transfer coefficient distribution. Figures 14b

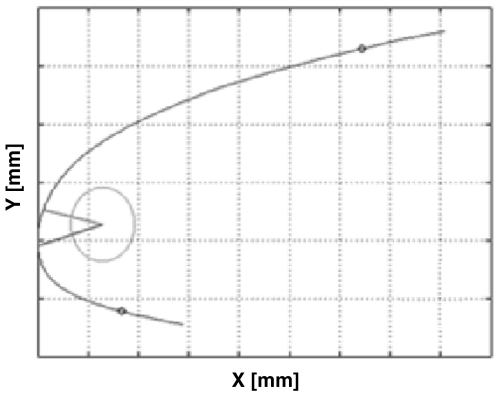

a) Piccolo geometry configuration

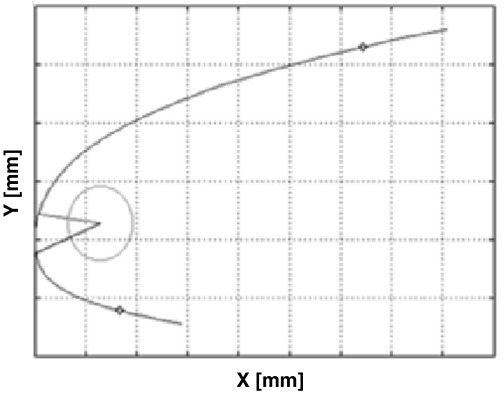

b) Piccolo geometry configuration

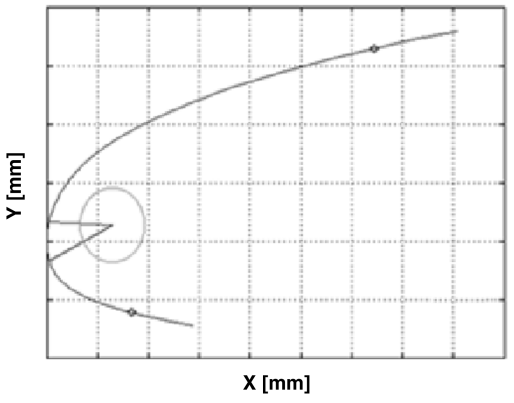

c) Piccolo geometry configuration

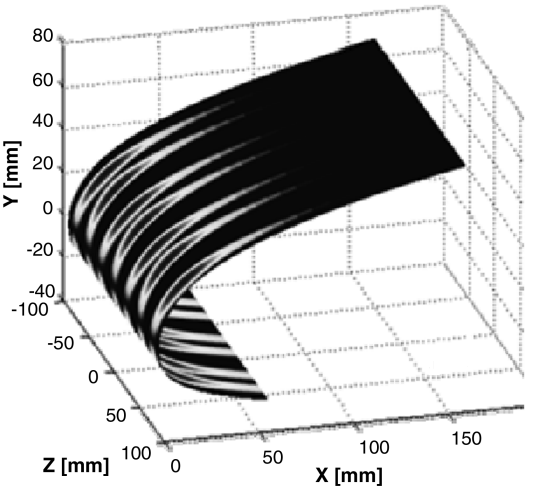

d) Water runback mass flow rate surface distribution

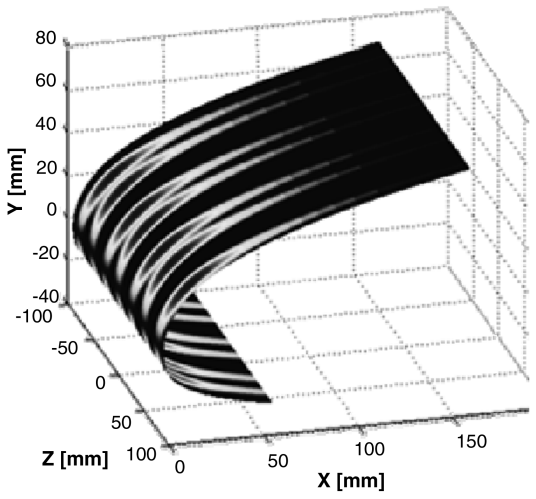

e) Water runback mass flow rate surface distribution

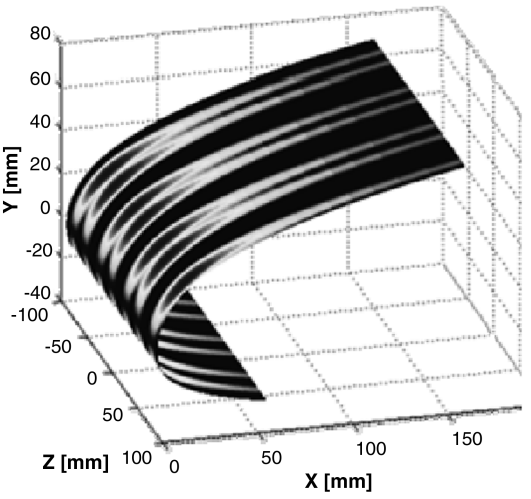

f) Water runback mass flow rate surface distribution

Fig. 17 Optimal design configuration versus off-design configurations.

and 14c present the computed surface temperature distribution and the anti-icing heat flux distribution associated to the geometric configuration. Figure 14d shows the distribution of evaporated water. Figure 14e presents the water runback on the airfoil skin, whose corresponding film thickness is shown in Fig. 14f.

F. Validation Results

Two sets of icing tunnel experimental data obtained over the currently used generic swept wing were available and provided by Bombardier Aerospace. These data consist in temperature sensor data taken over a cut on the wing surface located in-between two consecutive Piccolo holes, and compiled for two different test conditions. The first set was obtained in dry air condition (with zero LWC) and the second one in wet-air condition.

These icing experimental test cases were treated as test cases for the models presented in the preceding sections, in the sense that the corresponding numerical solutions were computed according to the methodology. Strictly speaking, the internal heat transfer coefficient distributions were directly extracted from the internal flow three-dimensional CFD computations, and the version of the water film solver included the transversal (spanwise) conduction.

Comparison between experimental and numerical results is presented in Fig. 15.

The numerical results revealed quite acceptable match with the experimental results, particularly in the region located in the vicinity of the jets impact zones where the relative error is within $\pm 3\%$. Some discrepancies occurred toward the upper (relative error up to 8 and 5% for the dry-and wet-air conditions) and lower (relative error up to 13 and 8%, respectively) ends of the slat. These discrepancies are attributed on the one hand to the difficulty of accurately computing the internal flow through the slot and rear bay because of geometry simplification (stiffeners were virtually removed for the feasibility of the mesh which increased the cross section at the level of the slot and therefore decrease the mass flow rate and thus the heat exchange), and on the other hand due to the presence of the exhaust flow and conduction through the stiffener, as illustrated in Fig. 4, which were not introduced in the numerical model.

The remaining discrepancies can be attributed to the simplifying assumptions of the water film model which do not account for certain features, such as the effect of rivulet flow described in the previous section or the slight spanwise component of the water runback, especially in the vicinity of the stagnation point, due to the three-dimensionality of the flow over the swept wing.

V. Results

Figure 16 illustrates the typical convergence behavior of the GA. The bold dots in Fig. 16a show the evolution of the best individual from generation to generation, which gradually converges toward the global optimum. The thin dots represent the average of the population, which also gradually evolves toward the best individual. In Fig. 16b, the mean distance between individuals tends to decrease as the generation number grows. In fact, the population is initially uniformly distributed across the design space using the Lp-τ method and will gradually contract and converge toward the global optimum, as summarized in Fig. 16c which shows the evolution of the mean value and range of the population with the generations.

To illustrate the subtleties of Piccolo tube optimization with fixed available anti-icing power, Fig. 17 presents three Piccolo tube configurations (see Figs. 17a–17c) with their associated water runback solutions (see Figs. 17d–17f). The Piccolo tube geometric configurations are shown in side view, with two lines showing the jets

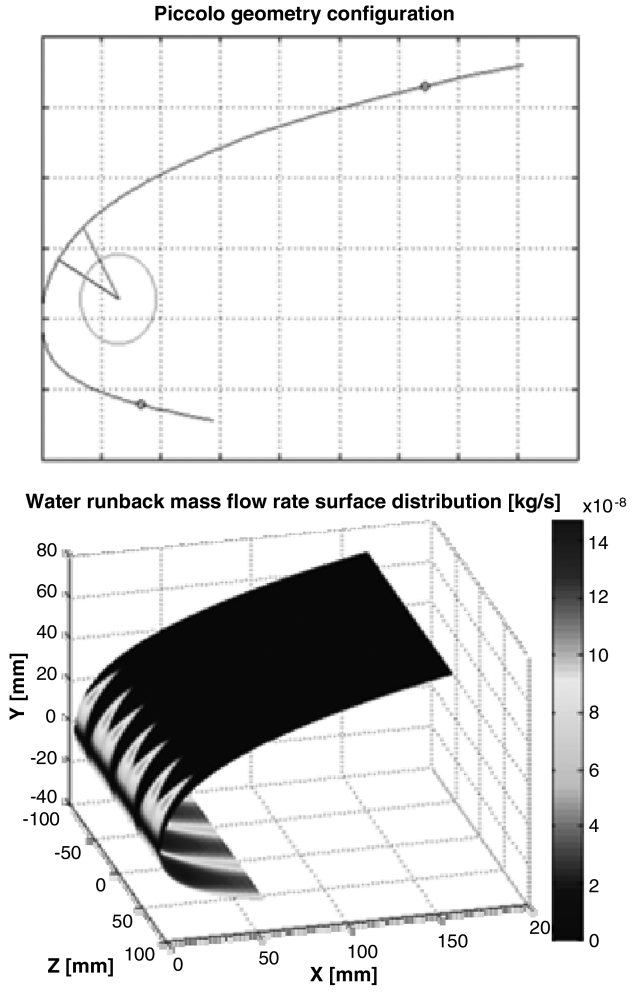

Fig. 18 Initial generic configuration (top) and corresponding water runback (bottom).

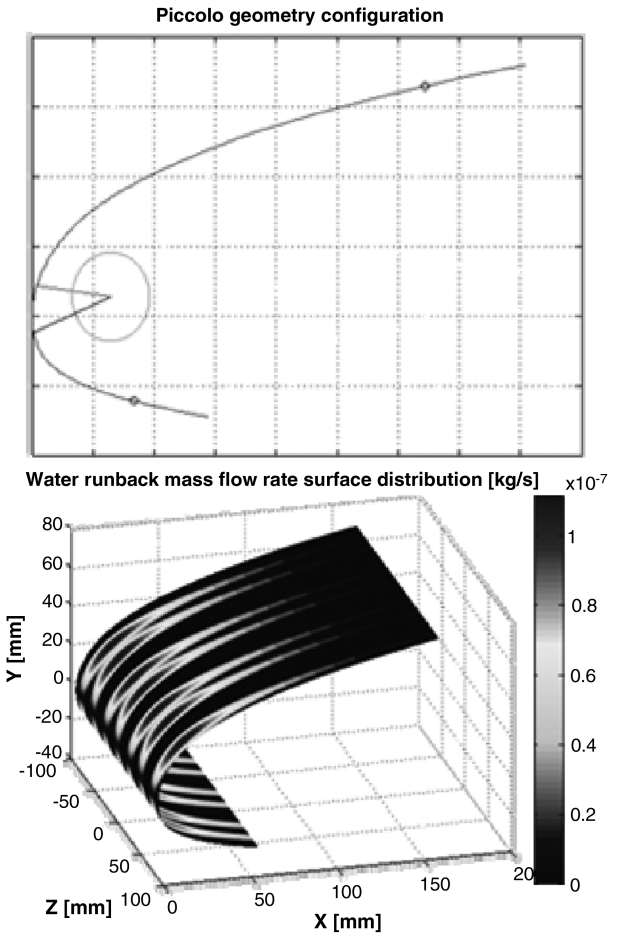

Fig. 19 Three-design-variable optimal configuration and corresponding water runback.

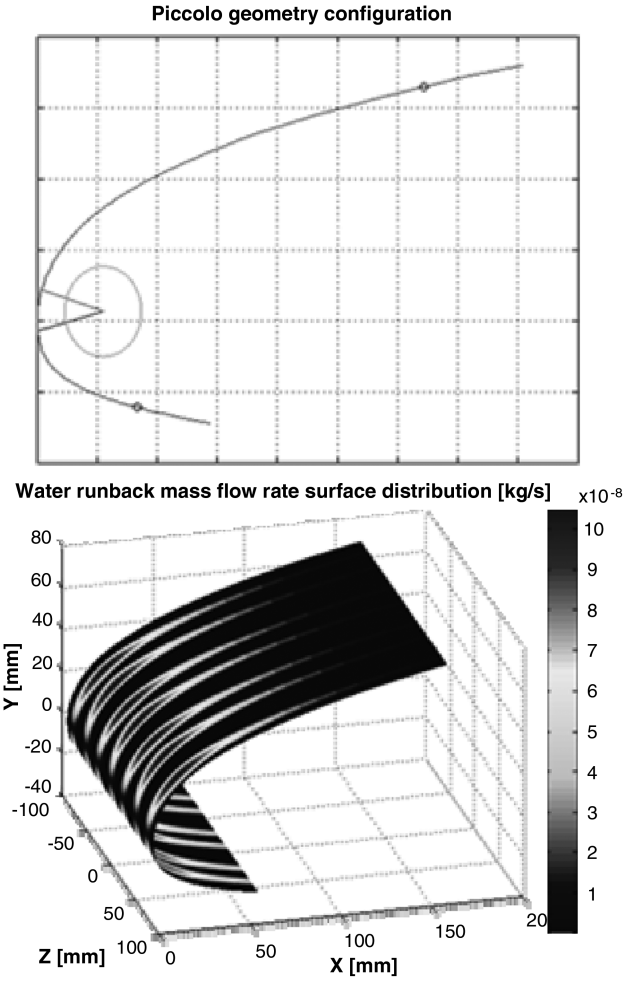

Fig. 20 Four-design-variable optimal configuration and corresponding water runback.

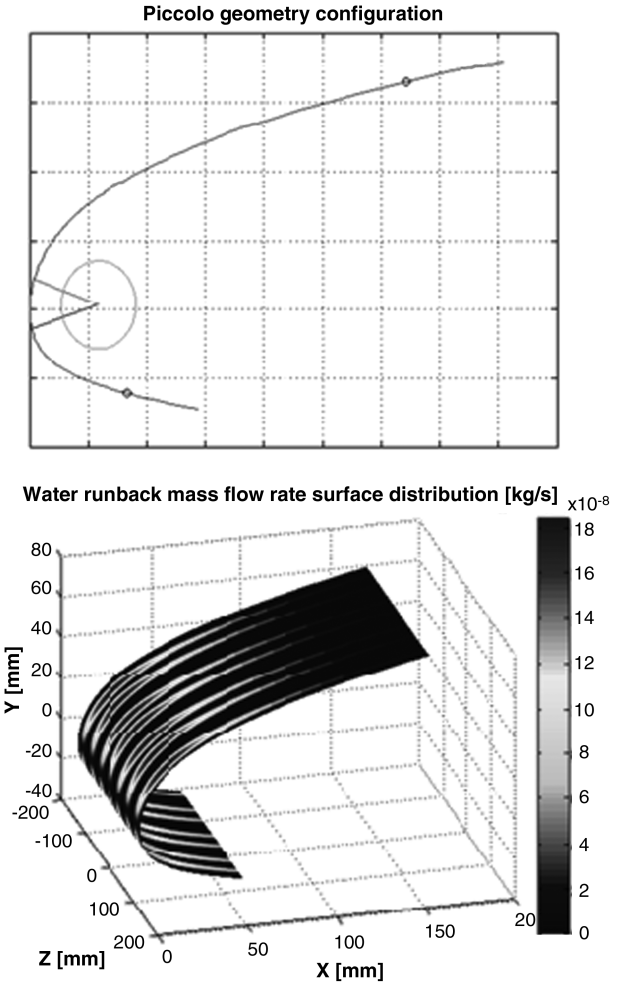

Fig. 21 Five-design-variable optimal configuration and corresponding water runback.

orientations. The ends of the heated zone are also materialized on the airfoil.

For this particular in-flight icing condition, the given anti-icing enthalpy was not high enough to achieve fully-evaporative condition on both upper and lower surfaces in any configuration within the range of design variables. Therefore, the lower surface minimum water runback criterion, mentioned in Sec. III.C, was used.

The second configuration in Fig. 17b refers to the optimal configuration in the case of three design variables (jet angles and distance between holes). It shows fully-evaporative conditions near the end of the upper heated surface with minimal runback out of the lower heated surface, as shown in Fig. 17e. Configurations 1 and 3 correspond to slight variations about the optimal point. On the one hand, the first configuration (see Fig. 17a) leads to stronger evaporative conditions on the upper heated surface, but to more runback on the lower heated surface (see Fig. 17d). On the other hand, the third configuration (Fig. 17c) leads to water runback on both upper and lower surfaces (see Fig. 17f). It is important to note that for all three configurations, the available anti-icing power (in terms of Piccolo tube air temperature and mass flow rate), is identical.

The results for the three, four and five design variables are presented for different arrangements and compared with the initial generic configuration (see Fig. 18).

These results consist of the optimal geometric configurations in the context of this particular single-objective optimization and within the range of the design variables. The arrangement for three design variables contains the two jet angles and the distance between holes (see Fig. 19). The arrangement for four design variables contains the two jet angles and the x- and y positions of the Piccolo tube (see Fig. 20). For all these arrangements, the parameters which are not used as design variables are kept identical to the initial generic configuration. Finally, the arrangement for five design variables combines all Piccolo tube geometric parameters (see Fig. 21).

The different configurations are summarized in Table 1. The first two columns give the values of the jet angles. The next one provides the value of the distance between adjacent holes, and the next two columns address the location of the Piccolo tube axis inside the slat. The last column shows the amount of water runback out of the heated zone, in milligrams per second and per meter of span. For the three optimized configurations, it corresponds to the amount of water runback on the lower surface only because fully-evaporative condi-

Table 1 Summary of the different optimal configurations compared with initial generic design

Configuration	θ_1	$\theta_2 - \theta_1$	c, mm	X_{pic}	Y_{pic}	m_{rb}, mg/s/m
Total impingement	——	——	——	——	——	978.4
Generic	30°	30°	50	25	5	203.3
Three design variables	−15.3°	30°	50	22.1	2.5	39.19
Four design variables	−8.6°	37.3°	50	23.2	2.1	26.29
Five design variables	−17.8°	36.6°	74.4	23.6	1.1	23.03

tions are met on the upper surface. The first line gives the value of the amount of water impinging on the slat, in order to get a sense of how much the system can evaporate. The values of the initial generic configuration's parameters are specified in the next line and the optimized configurations are presented in the last three lines.

For this particular design case, the computed amount of water runback for the initial generic configuration was 203.3 mg/s/m of span for a total amount of water droplet impingement of 978.4 mg/s/m of span. For three design variables, the optimal configuration led to a reduction of the water runback by a factor of 5.19 (i.e., the amount of water runback was divided by a factor of 5.19 with respect to the generic case). The reduction factor is defined as the ratio of the amount of water runback for the generic configuration over the one for the optimal configuration. For four design variables, the optimal configuration led to a reduction of the water runback by a factor of about 7.73. Finally, for five design variables, the obtained optimal configuration led to a reduction of the water runback by a factor of 8.83.

Logically, releasing an additional degree of freedom, i.e., adding a design variable, will lead to a "better" optimum. In reality, the optimal configuration of the subspace might only be a local optimum of the higher-dimension space. It is actually the most probable case because the subspace is constrained arbitrarily with respect to the remaining design variables. The tendency of increasing optimality, shown by using ROM for three and four design variables, has been verified by carrying out the calculation for five design variables without ROM (i.e., computing each individual solution by means of the water film model). Thus, further increasing the number of design variables keeps on improving the optimal configuration until it would asymptotically reach the "true" optimum, however, at a highly increasing computational cost with the growth of the design space. Therefore, selecting only the most critical parameters as design variables (via a sensitivity analysis such as presented in [25]), would enhance the "quality" of the optimum to computation time ratio.

In this study, the optimization was not done sequentially, because for each of these configurations the GA was reinitialized to a uniformly distributed initial population. Sequential optimization was investigated, however, with moderate results only. Indeed, starting from the lower-dimension optimal GA population results would not necessarily lead to significant improvement, even if the population is uniformly spread in the supplementary dimension. This bias in the GA initial population could lead to the convergence toward a local optimum and therefore would not guaranty convergence toward the best possible optimum of the constrained design space. It would even result in a more laborious convergence, because it would require a higher rate of mutation to recover the necessary diversity in the population.

VI. Conclusions

This paper attempts to bring some rigor to a field long governed by trial-and-error and empiricism. It presents an optimization methodology for hot-air anti-icing systems combining GAs, which are ideal for searching multidimensional design space, with a powerful POD-based ROM allowing to greatly reducing the computational cost. Being both affordable and modular, this optimization method is promising and adaptable to handle more complex three-dimensional geometries and physics. This method was successfully applied and led to optimal geometric configurations for three-, four-, and five-dimensional design spaces, improving the initial generic design by up to about 883%.

In terms of future developments, geometric shape and variations in Piccolo power inputs in the spanwise direction can be taken into account, as well as wing tip and root effects. The ROM module can be upgraded to improve the accuracy. Moreover, the correlation can be first replaced by POD-based CFD computations of the internal flow before upgrading back to direct three-dimensional CFD computation. On the other hand, the water film model can be replaced by the ICE3D module of FENSAP-ICE. Also, the use of a hybrid optimization method combining GAs for the first phase of design space search to a gradient-based method in a second phase is to be investigated for a more efficient optimization framework.

Further research could focus on applying the ROM directly to fully-coupled computations constituting the snapshots, and running the GA module with such a higher-fidelity POD model. An interesting future application would be to adapt this method to electro-thermal anti-icing systems.

Acknowledgment

This project was graciously funded by the Natural Sciences and Engineering Research Council of Canada–J. Armand Bombardier–Bell Helicopter–CAE Industrial Research Chair for Multidisciplinary Computational Fluid Dynamics.

References

[1] "Annual Review of Aircraft Accident Data," U.S. General Aviation National Transportation Safety Board Rept. NTSB/ARC-09-01, 2005.

[2] Petty, K. R., and Floyd, C. D. J.," A Statistical Review of Aviation Airframe Icing Accidents in the US," 11th American Society for Microbiology Conference on Aviation, Range, and Aerospace, Hyannis, MA, 2004.

[3] Cober, S. G., and Isaac, G. A.," Aircraft Icing Environments Observed In Mixed-Phase Clouds," 40th AIAA Aerospace Sciences Meeting and Exhibit, Reno, NV, AIAA 2002-675, 2002.

[4] Steuernagle, J., Roy, K., and Wright, D., "Safety Advisor: Aircraft Icing," Aircraft Owners and Pilots Association Air Safety Foundation, 2008.

[5] Federal Aviation Administration, "Airworthiness Standards: Transport Category Airplanes, Part 25, Appendix C," 2007.

[6] European Aviation Safety Agency, "Certification Specifications for Large Aeroplanes CS-25, Appendix C," 2003.

[7] Transport Canada, 2009.

[8] Yeoman, K. E., "Efficiency of a Bleed Air Powered Inlet Icing Protective System," 32nd AIAA Aerospace Sciences Meeting and Exhibit, Reno, NV, AIAA Paper 1994-717, 1994.

[9] Norris, R. M., Rumford, K. J., and Youd, D. S., Avco Corporation, Providence, RI, U.S. Patent No. 4831819 for a "Anti-Icing Valve," filed 07 Feb. 1987.

[10] Wang, H., Tran, P., Habashi, W. G., Chen, Y., Zhang, M., and Feng, L., "Anti-Icing Simulation in Wet Air of a Piccolo System using FENSAP-ICE," 2007 Society of Automotive Engineers Aircraft and Engine Icing International Conference, Society of Automotive Engineers Paper 2007-01-3357, Seville, Spain, 2007.

[11] Pueyo, A., Mokhtarian, F., and Kafyeke, F., "Validation of a Hot-Air Anti-Icing Simulation Code," Society of Automotive Engineers World Aviation Congress and Exposition, Montreal, Society of Automotive Engineers Paper 2003-01-3031, 2003.

[12] Lee, J., Rigby, D., Wright, W., and Choo, Y., "Analysis of Thermal Ice Protection System (TIPS) with Piccolo Tube Using State-of-the-Art Software," 44th AIAA Aerospace Sciences Meeting and Exhibit, Reno, NV, AIAA Paper 2006-1011, 2006.

[13] Liu, H. H. T., and Hua, J., "Three-Dimensional Integrated Thermodynamic Simulation for Wing Anti-Icing System," *Journal of Aircraft*, Vol. 41, No. 6, 2004, pp. 1291–1297. doi:10.2514/1.5594

[14] Hua, J., and Liu, H. H. T., "Fluid Flow and Thermodynamic Analysis of a Wing Anti-Icing System," *Canadian Aeronautics and Space Journal*, Vol. 51, No. 1, 2005, pp. 35–40.

[15] Huber, A. M., and Viskanta, R., "Effect of Jet–Jet Spacing on Convective Heat Transfer to Confined, Impinging Arrays of Axisymmetric Air Jets," *International Journal of Heat and Mass Transfer*, Vol. 37, No. 18, 1994, pp. 2859–2869. doi:10.1016/0017-9310(94)90340-9

[16] San, J.-Y., Lai, M.-D., "Optimum Jet-to-Jet Spacing of Heat Transfer for Staggered Arrays of Impinging Air Jets," *International Journal of Heat and Mass Transfer*, Vol. 44, No. 21, 2001, pp. 3997–4007. doi:10.1016/S0017-9310(01)00043-6

[17] Rhee, D.-H., Yoon, P.-H., and Cho, H. H., "Local Heat/Mass Transfer and Flow Characteristics of Array Impinging Jets with Effusion Holes Ejecting Spent Air," *International Journal of Heat and Mass Transfer*, Vol. 46, No. 6, 2003, pp. 1049–1061. doi:10.1016/S0017-9310(02)00363-0

[18] Fregeau, M., Saeed, F., and Paraschivoiu, I., "Numerical Heat Transfer Correlation for Array of Hot-Air Jets Impinging on Three-Dimensional Concave Surface," *Journal of Aircraft*, Vol. 42, No. 3, 2005, pp. 665–

670.
doi:10.2514/1.3856
[19] Rama Kumar, B. V. N., Prasad, B. V. S. S. S., "Computational Flow and Heat Transfer of a Row of Circular Jets Impinging on a Concave Surface," *Heat and Mass Transfer*, Vol. 44, No. 6, 2008, pp. 667–678 doi:10.1007/s00231-007-0274-3.
[20] Planquart, P., Vanden Borre, G., and Buchlin, J.-M., "Experimental and Numerical Optimization of a Wing Leading Edge Hot Air Anti-Icing System," 43rd AIAA Aerospace Sciences Meeting and Exhibit, Reno, NV, AIAA Paper 2005-1277, 2005.
[21] Wright, W. B., "An Evaluation of Jet Impingement Heat Transfer Correlations for Piccolo Tube Application," 42nd AIAA Aerospace Sciences Meeting and Exhibit, Reno, NV, AIAA Paper 2004-62, 2004.
[22] Brown, J. M., Raghunathan, S., Watterson, J. K., Linton, A. J., and Riordon, D., "Heat Transfer Correlation for Anti-Icing Systems," *Journal of Aircraft*, Vol. 39, No. 1, 2002, pp. 65–70. doi:10.2514/2.2896
[23] Wong, S.-H., Papadakis, M., and Zamora, A., "Computational Investigation of a Bleed Air Ice Protection System," First AIAA Atmospheric and Space Environments Conference, San Antonio, TX, AIAA Paper 2009-3966, 2009.
[24] Rigby, D., "Numerical Investigation of Hole Pattern Effect on Piccolo Tube Anti-Icing," 44th AIAA Aerospace Sciences Meeting and Exhibit, Reno, NV, 2006.
[25] Santos, L. C. d. C., Domingos, R. H., Maria, R. B., and Leal, M. d. F., "Sensitivity Analysis of a Bleed Air Anti-Ice Thermal Model to Geometrical and Operational Parameters," 46th AIAA Aerospace Sciences Meeting and Exhibit, Reno, NV, AIAA Paper 2008-445, 2008.
[26] Papadakis, M., Wong, S.-H., Yeong, H.-W., Wong, S.-C., and Vu, G. T., "Icing Tunnel Experiments with a Hot Air Anti-Icing System," 46th AIAA Aerospace Sciences Meeting and Exhibit, Reno, NV, 2008.
[27] Saeed, F., and Paraschivoiu, I., "Optimization of a Hot-Air Anti-Icing System," 41st AIAA Aerospace Sciences Meeting and Exhibit, Reno, NV, AIAA Paper 2003-733, 2003.
[28] Bombardier Aerospace proprietary data (2009).
[29] Man, K. F., Tang, K. S., and Kwong, S., "Genetic Algorithms: Concepts and Applications," *IEEE Transactions on Industrial Electronics*, Vol. 43, No. 5, 1996, pp. 519–534. doi:10.1109/41.538609
[30] Whitley, D., "A Genetic Algorithm Tutorial," *Statistics and Computing*, Vol. 4, No. 2, 1994, pp. 65–85.
[31] Van den Braembussche, R. A., "Tuning of Optimization Strategies," NATO Research and Technology Organization Lecture Series (AVT-167) on "Strategies for Optimization and Automated Design of Gas Turbine Engines," Montreal, 26–27 Oct. 2009.
[32] Arizono, H., and Isogai, K., "Application of Genetic Algorithm for Aeroelastic Tailoring of a Cranked-Arrow Wing," *Journal of Aircraft*, Vol. 42, No. 2, 2005, pp. 493–499. doi:10.2514/1.392
[33] Tahara, Y., Tohyama, S., and Katsui, T., "CFD-Based Multi-Objective Optimization Method for Ship Design," *International Journal for Numerical Methods in Fluids*, Vol. 52, No. 5, 2006, pp. 499–527. doi:10.1002/fld.1178
[34] Chung, H.-S., and Alonso, J. J., "Multiobjective Optimization Using Approximation Model-Based Genetic Algorithms," 10th AIAA/International Society for Structural and Multidisciplinary Optimization Symposium on Multidisciplinary Analysis and Optimization, Albany, NY, AIAA Paper 2004-4325, 2004.
[35] Jeong, S., Murayama, M., and Yamamoto, K., "Efficient Optimization Design Method Using Kriging Model," *Journal of Aircraft*, Vol. 42, No. 2, 2005, pp. 413–420. doi:10.2514/1.6386
[36] Van den Braembussche, R. A., "Evolutive Methods: Theoretical Aspects and Definitions," NATO Research and Technology Organization Lecture Series (AVT-167) on "Strategies for Optimization and Automated Design of Gas Turbine Engines," Montreal, 26–27 Oct. 2009.
[37] Lepot, I., "Introduction and Terminology," NATO Research and Technology Organization Lecture Series (AVT-167) on "Strategies for Optimization and Automated Design of Gas Turbine Engines," Montreal, 26–27 Oct. 2009.
[38] Burkardt, J., Gunzburger, M., and Lee, H.-C., "POD and CVT-Based Reduced-Order Modeling of Navier–Stokes Flows," *Computer Methods in Applied Mechanics and Engineering*, Vol. 196, Nos. 1–3, 2006, pp. 337–355. doi:10.1016/j.cma.2006.04.004
[39] Li, G., Li, M., Azarm, S., Rambo, J., and Joshi, Y., "Optimizing Thermal Design of Data Center Cabinets with a New Multi-Objective Genetic Algorithm," *Distributed and Parallel Databases*, Vol. 21, Nos. 2–3, 2007, pp. 167–192.
[40] Coelho, R. F., Breitkopf, P., and Knopf-Lenoir, C., "Model Reduction for Multidisciplinary Optimization: Application to a Two-Dimensional Wing," *Structural and Multidisciplinary Optimization*, Vol. 37, No. 1, 2008, pp. 29–48. doi:10.1007/s00158-007-0212-5
[41] Lepot, I., "Complements on Surrogate Based Optimization for Engineering Design," NATO Research and Technology Organization Lecture Series (AVT-167) on "Strategies for Optimization and Automated Design of Gas Turbine Engines," Montreal, 26–27 Oct. 2009.
[42] Holmes, P., Lumley, J. L., and Berkooz, G., *Turbulence, Coherent Structures, Dynamical Systems and Symmetry: Proper Orthogonal Decomposition*, Cambridge Univ. Press, New York, 1996, pp. 86–117, Chap. 3.
[43] Liang, Y. C., Lee, H. P., Lim, S. P., Lin, W. Z., Lee, K. H., and Wu, C. G., "Proper Orthogonal Decomposition and its Applications. Part 1: Theory," *Journal of Sound and Vibration*, Vol. 252, No. 3, 2002, pp. 527–544. doi:10.1006/jsvi.2001.4041
[44] Sirovich, L., "Turbulence and the Dynamics of Coherent Structures. Part 1: Coherent Structures," *Quarterly of Applied Mathematics*, Vol. 45, No. 3, 1987, pp. 561–571.
[45] Lappo, V., and Habashi, W. G., "POD-Kriging Approximations of Multi-Disciplinary CFD Simulation with Application to In-Flight Icing," 17th Annual Conference of the Computational Fluid Dynamics Society of Canada, Ottawa, ON, Canada, Computational Fluid Dynamics Society of Canada Paper CFDSC2009-6E3, 2009.
[46] Isaacs, A., "Sampling Strategies for Computer Experiments," CASDE TR 04-01, Jan. 2004.
[47] Sobol, I. M., "On the Systematic Search in a Hypercube," *SIAM Journal on Numerical Analysis*, Vol. 16, No. 5, 1979, pp. 790–793. doi:10.1137/0716058
[48] Statnikov, R. B., and Matusov, J. B., *Multicriteria Optimization and Engineering*, Chapman and Hall, New York, 1995, p. 212.
[49] Habashi, W. G., "Recent Advances in CFD for In-Flight Icing Simulation," *Japan Society of Fluid Mechanics*, Vol. 28, No. 2, 2009, pp. 99–118.
[50] Pellissier, M. P. C., "Optimization via CFD of Aircraft Hot-Air Anti-Icing Systems," Masters Thesis, Dept. of Mechanical Engineering, McGill Univ., Montreal, 2010.
[51] Saeed, F., Morency, F., and Paraschivoiu, I., "Numerical Simulation of a Hot-Air Anti-Icing System," 38th AIAA Aerospace Sciences Meeting and Exhibit, Reno, NV, AIAA Paper 2000-630, 2000.
[52] Goldstein, R. J., Behbahani, A. I., and Kieger Heppelmann, K., "Streamwise Distribution of the Recovery Factor and the Local Heat Transfer Coefficient to an Impinging Circular Air Jet," *International Journal of Heat and Mass Transfer*, Vol. 29, No. 8, 1986, pp. 1227–1235. doi:10.1016/0017-9310(86)90155-9
[53] Messinger, B. L., "Equilibrium Temperature of an Unheated Icing Surface as a Function of Airspeed," *Journal of Aeronautical Sciences*, Vol. 20, No. 1, 1953, pp. 29–42.
[54] Myers, T. G., "Extension to the Messinger Model for Aircraft Icing," *AIAA Journal*, Vol. 39, No. 2, 2001, pp. 211–218. doi:10.2514/2.1312
[55] Lima da Silva, G. A., de Mattos Silvares, O., and Godoy de Jesus Zerbini, E. J., "Numerical Simulation of Airfoil Thermal Anti-Ice Operation, Part 1: Mathematical Modeling," *Journal of Aircraft*, Vol. 44, No. 2, 2007, pp. 627–634. doi:10.2514/1.544